33.6 A Millimetric Batteryless Biosensing and Stimulating Implant with Magnetoelectric Power Transfer and 0.9pJ/b PWM Backscatter

Zhanghao Yu*, Huan-Cheng Liao*, Fatima Alrashdan, Ziyuan Wen, Yiwei Zou, Joshua Woods, Wei Wang, Jacob T. Robinson, Kaiyuan Yang

Rice University, Houston, TX
*Equally Credited Authors (ECAs)

2024 IEEE International Solid-State Circuits Conference (ISSCC) | 979-8-3503-0620-0/24/$31.00 ©2024 IEEE | DOI: 10.1109/ISSCC49657.2024.10454271

Bioelectronic implants transform clinical therapies by offering unprecedented tools for precise sensing and intervention inside the human body. Wireless, battery-free, and miniaturized (mm-scale) bio-implants are highly desirable to enhance safety, simplify surgery, minimize behavioral disruptions, and boost long-term stability over conventional bulky implants [1-3]. Developing such devices faces two crucial challenges: safe and reliable wireless power transfer (WPT) and efficient bidirectional telemetry. Magnetoelectric (ME) WPT, which converts low-frequency magnetic fields to electrical energy via acoustic coupling (Fig. 33.6.1, top), is an emerging WPT modality specialized for mm-sized implants. It offers strong penetration through various mediums without absorption or reflection issues, leading to superior WPT efficiency, power level under safety limits, and misalignment tolerance, all of which have been demonstrated in large animal models [1]. However, uplink telemetry in ME-powered implants, essential for real-time sensing and closed-loop physiological control, remains challenging. Integrating a second antenna, such as an inductive coil, is a straightforward solution to add uplink to ME implants [4], but it increases the implant size and complicates integration. Sharing a single transducer for power and data is highly desirable for device miniaturization, as demonstrated in inductive coupling and ultrasound [2]. Two recent studies [5,6] have explored the converse ME effects to realize ME uplink (Fig. 33.6.1, middle). The feasibility of directly driving an ME transducer with AC voltages for uplink is reported in [5], but due to the kΩ-impedance of ME transducers, this method consumes significant power for a batteryless implant. On the other hand, [6] demonstrates low-power ME backscatter using load shift keying (LSK) based on an observation that changing the passive load to an ME transducer during its ringdown modulates its vibration frequency. The high-Q ME transducer vibrates for more than 30 cycles after turning off the excitation magnetic field. Despite the exciting progress, LSK ME backscatter has limited SNR and data rate, due to the ME transducer's high Q. Specifically, SNR is limited by a direct trade-off between frequency shift and signal strength, while the data rate is limited by the relatively long excitation and ringdown periods.

Towards a faster and more reliable uplink for ME implants, this paper presents PWM ME backscatter enabled by switched-capacitor energy extraction (SCEE), which quickly dissipates energy in an ME transducer and reduces the amplitude of the backscattered signal (Fig. 33.6.1, bottom). Compared to the FSK method [5], time-domain PWM backscatter offers higher SNR and encodes multiple bits in a single ringdown phase. Based on this principle, we built a prototype system including a 6.7mm^3 ME implant and a custom portable transceiver (TRX) for wireless recording and stimulation. The implant SoC integrates power management, bidirectional data transmission, bio-stimulation, temperature sensing, and LFP/EGM/ECG recording (Fig. 33.6.2, top). Our system features: (1) wireless power, downlink, and PWM backscatter uplink using a single 5×2×0.2mm^3 ME transducer within the implant; (2) SCEE reducing the backscattered signal amplitude by >50% within 2 ME cycles for high-SNR PWM; (3) PWM ME backscatter achieving 17.73kb/s data rate and 0.9pJ/b efficiency at 331kHz carrier; (4) reliable wireless operation at up to 5cm distance, with <8.5×10^{-5} BER using lightweight multi-layer-perceptron (MLP) demodulation.

To achieve fast amplitude reduction on the backscattered signal, we draw inspiration from the Synchronized-Switch-Harvesting-on-Capacitors design for energy harvesting [7] to develop the SCEE technique for quick energy dissipation (Fig. 33.6.2, bottom). SCEE uses a sequentially activated switched-capacitor array to extract energy from the piezoelectric-layer capacitor C_p at the peak points of the sinusoidal ME signal when C_P holds the peak energy. Compared to the switched-inductor alternative, the switched-capacitor approach does not require reverse current sensing, is less sensitive to switch on-resistance, and allows on-chip integration, making it more suitable for our miniaturized ME implant. Besides the SCEE, the TX module comprises a peak detector (PD) and a baseband and timing controller. An accurate, low-power PD is essential for achieving the expected bandwidth and efficiency of the PWM ME backscatter. Different from conventional PDs for energy harvesters, the PD for ME backscatter works with a ringdown waveform decaying over time, operates at a much higher frequency (331kHz in our design versus <1KHz in energy harvesters), and suffers from varying input amplitudes caused by the uncertain wireless channel. The conventional active-diode PD necessitates high input voltage, track & hold PD requires a wide-bandwidth amplifier, and voltage-to-current conversion PD demands a series capacitor and constant current reference which can be sensitive to parasitic and input variation. Here, we developed a specialized high-performance low-power PD by combining zero-crossing detection and phase shifting, exploiting the fact that detecting zero points is easier and more accurate, and peak points are always 90° and 270° away from the zero points in a sine wave.

Figure 33.6.3 details the Peak Detector, which works in two modes: calibration and data transmission. At the beginning of each uplink session, the digital phase shifter (DPS) within PD is calibrated to the ME cycle time T_{ME} by operating DPS as a TDC. After calibration, TX enters data transmission mode, and PD starts to produce peak-aligned pulse trains (EN_{SCEE}) for controlling the SCEE. Here, PD adds $T_{ME}/4$ and $3T_{ME}/4$ delays to the output pulse of the zero-crossing detector (ZCD) to locate positive (P_{PP}) and negative (P_{NP}) peaks. To minimize energy, PD is only activated for 4 ME cycles by the baseband controller, which tracks the number of ringdowns and ME clock over the entire uplink session. Within these 4 cycles, ZCD is activated only in the first cycle while DPS creates 8 EN_{SCEE} pulses based on its calibrated delay line, lowering the total average power to 15nW. For accurate detection, ZCD uses a comparator with an intentionally added offset current, which minimizes detection delay by intentionally adding an offset without significantly increasing the biasing current. However, using a fixed sinking current I_1 leads to overcompensation at later ME ringdown cycles with smaller amplitudes. Our solution is adding a sourcing current I_2 increasing with cycles to I_1, yielding a significantly reduced and more consistent ZCD delay. I_2 is biased by an ME envelope extractor that is also necessary for downlink. The DPS comprises a differential 4-stage folded delay chain with a 15ns step (i.e., 0.5% of T_{ME}), a cycle counter, sampling DFFs, and a digital pulse generator. The pulse generator is co-designed with the 4-stage delay chain to approximate $T_{ME}/4$ and $T_{ME}/2$ delays at minimum power and area overheads. The approximation error is at most 3/4 of the single-stage delay and does not affect SCEE performance.

We developed fully integrated prototypes of the ME implants with a 180nm CMOS SoC and a portable external TRX. The SoC includes a recording AFE and supports continuous data streaming. To achieve a higher input dynamic range, we employed a low-gain AC-coupled LNA and a third-order noise-shaping SAR ADC [8] with 1kHz bandwidth and an oversampling ratio of 8. ADC output is decimated by a 3-stage cascaded-integrator-comb filter and a delta modulator (to reduce data rate), resulting in a final 8b 2kSa/s data stream (Fig. 33.6.4, top).

We evaluated the function of the entire system *ex vivo* using a 2cm-thick porcine tissue. Figure 33.6.4 shows the implant being magnetoelectrically powered and programmed with time-domain modulated downlink data to perform different tasks including stimulation and uplink telemetry. The zoom-in views show that SCEE extracts the ME transducer's energy at different time points during the ringdown based on PWM data. The prototype demonstrates energy extraction from the ME transducer near the optimal peak points, causing an immediate biasing flip. The 4-cycle energy extraction quickly dissipates the energy in the ME transducer, resulting in a >1V decrease in the transducer's output voltage. The first peak detection pulse shows an error of 18ns (i.e., 0.6% of T_{ME}), demonstrating sufficient accuracy of the PD.

The backscattered signal is demodulated by a custom ME backscatter RX including an AFE and an MCU (Fig. 33.6.5). The signal after RX AFE shows distinguishable pulse widths during ringdown, modulated by the 3b uplink data (Fig. 33.6.5, bottom left). Each 3b data packet takes a 24-ME-cycle excitation phase, succeeded by a 32-ME-cycle ringdown phase, resulting in a data rate of 17.73kb/s with a 331kHz carrier. Owing to fast amplitude reductions at accurate time intervals, the received signal achieves an SNR >10.9dB at up to 5cm distance. We designed and measured two data decoding algorithms, straightforward time-domain drop detection, and a tiny 4-layer neural network (MLP) with quantized 5b integer weights. The latter offers higher accuracy at greater distances with higher but acceptable computing power, yielding a BER of 8.5×10^{-5} at 5cm (Fig. 33.6.5, bottom right).

Finally, we evaluated the implant's wireless recording by feeding pre-recorded local field potentials (LFP) from rats to the device. The wirelessly received signal via PWM ME backscatter closely matches the ground truth (Fig. 33.6.6, top). Additionally, we *in vitro* validated an encapsulated untethered implant in phosphate-buffered saline (PBS), where power, data, and LFP signals are wirelessly transmitted through PBS. Figure 33.6.6 includes a comparison table with state-of-the-art wireless bio-implants with bidirectional communication. The SoC's power breakdown and die micrograph are in Fig. 33.6.7.

Acknowledgement:
This work is supported in part by the National Science Foundation (NSF) ASCENT and CAREER programs under Grant No. 2023849 and 2146476.

References:

[1] J.C. Chen, et al., "A Wireless Millimetric Magnetoelectric Implant for the Endovascular Stimulation of Peripheral Nerves," *Nat. Biomed. Eng.*, vol. 6, no. 6, pp. 706-716, 2022.
[2] M.M. Ghanbari, et al., "A Sub-mm^3 Ultrasonic Free-Floating Implant for Multi-Mote Neural Recording," *IEEE JSSC*, vol. 54, no. 11, pp. 3017-3030, Nov. 2019.
[3] J. Lee, et al., "Neural Recording and Stimulation Using Wireless Networks of Microimplants," *Nat. Electron.*, vol. 4, no. 8, pp. 604-614, Aug. 2021.
[4] Z. Yu et al., " A Wireless Network of 8.8-mm^3 Bio-Implants Featuring Adaptive Magnetoelectric Power and Multi-Access Bidirectional Telemetry," *RFIC*, pp. 47-50, 2022.

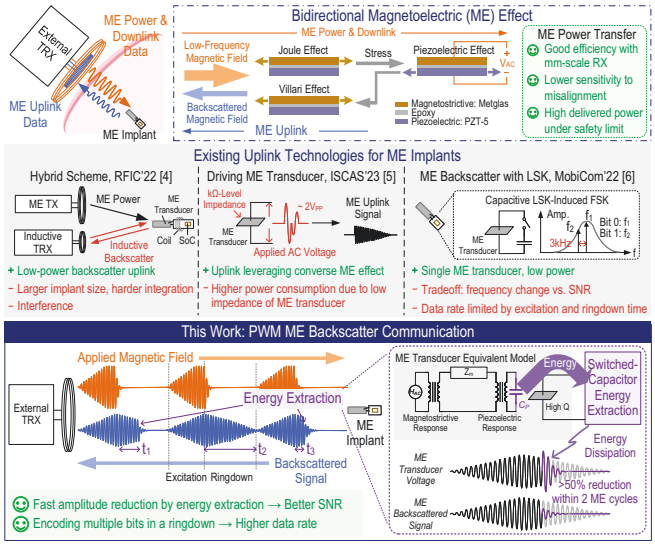

Figure 33.6.1: Conceptual diagram of a magnetoelectric (ME) implant using a single ME transducer for power and bidirectional data transfers; principles of PWM ME backscatter to enhance bandwidth and SNR over prior works.

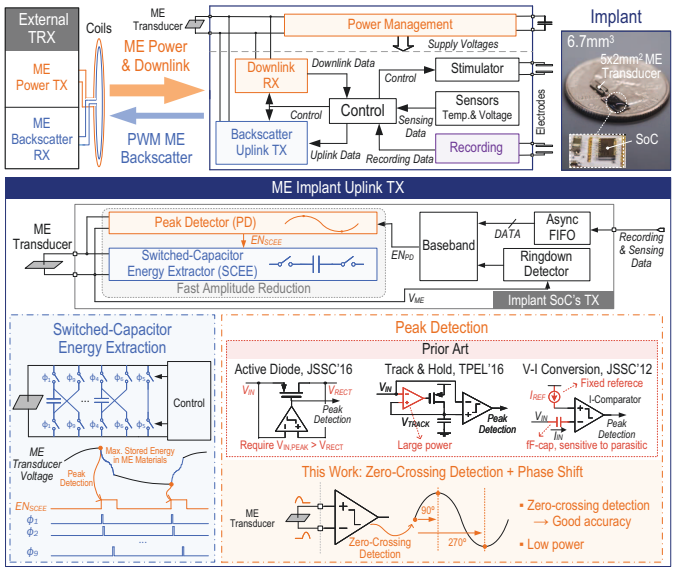

Figure 33.6.2: System diagram and a picture of the 6.7mm³ implant; illustrations of the PWM ME backscatter module and the key techniques SCEE and PD.

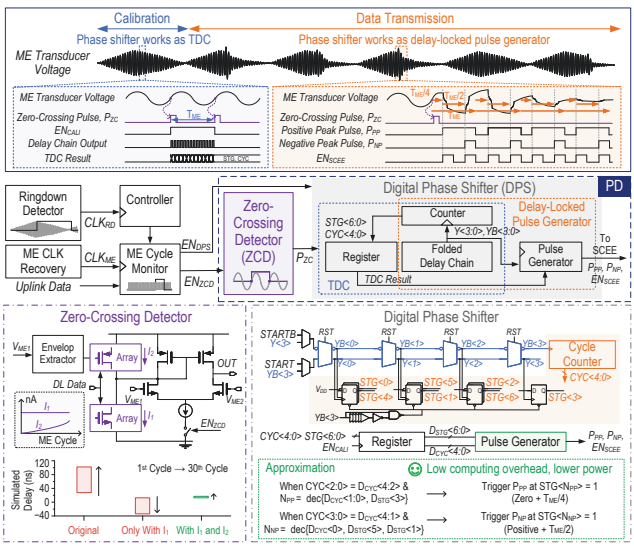

Figure 33.6.3: Operation waveforms and schematics of the peak detector (PD) circuits, including a ZCD with compensation current for delay reduction and a DPS with approximated digital pulse generation.

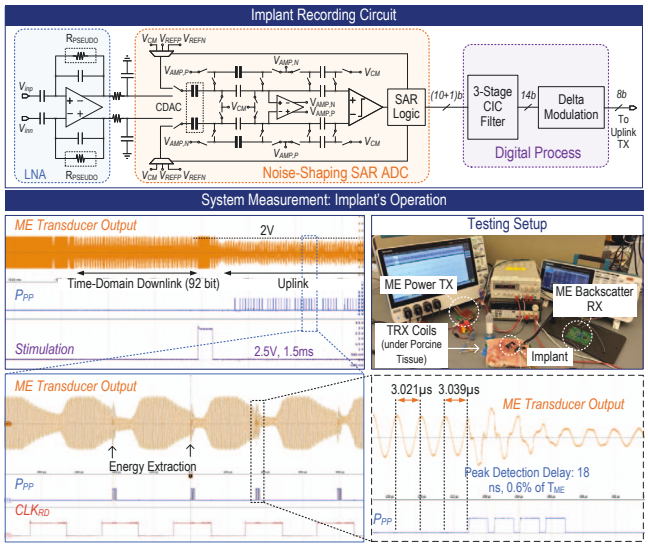

Figure 33.6.4: Schematic of the implant's recording frontend; *ex vivo* testing setup and measured implant operation waveform, with zoom-in views of the ME energy extraction process.

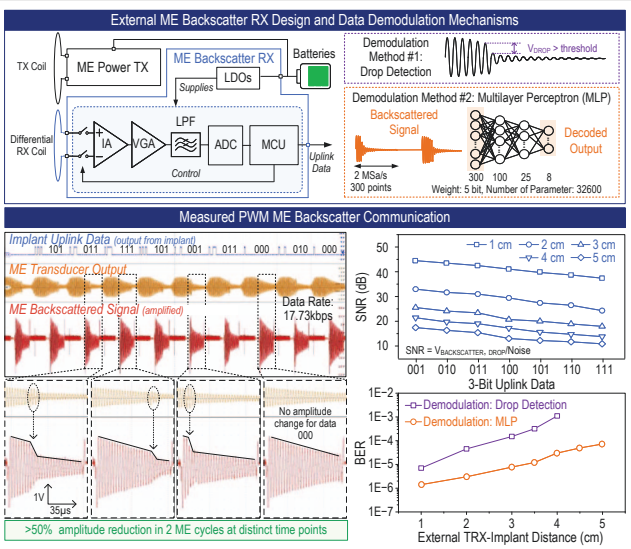

Figure 33.6.5: Diagrams of the portable external TRX; demodulation schemes for PWM ME backscatter; measured waveforms of PWM ME backscatter; and measured SNR and BER across distances.

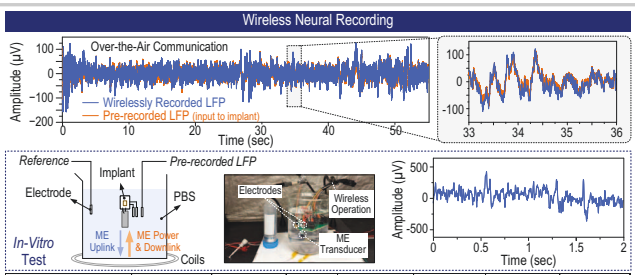

		This Work	Z. Yu MobiCom'22 [6]	J. Lim VLSI'21 [9]	J.Lee Nat. Elec.'21 [3]	Y. Jia ISSCC'20 [10]	S. Sonmezoglu ISSCC'20 [11]	M. Ghanbari JSSC'19 [2]
Biomedical Function		Stimulation, Recording	Stimulation	Recording	Recording	Stimulation, Recording	O_2 Sensing	Recording
SoC Technology (nm)		180	180	180	65	350	65	65
Power	Source	ME	ME	Photodiode	RF	Inductive	Ultrasound	Ultrasound
	Transfer Efficiency	0.37% (2cm)	0.2% (2cm)	N/A	0.08% (0.8cm)	N/A	N/A	0.06% (1.8cm)
Downlink Data	Modality	ME	ME	Photodiode	RF	Inductive	N/A	N/A
	Modulation	Time	Time	PWM	PWM	OOK		
Uplink Data	Modality	ME	ME	LED	RF	RF	Ultrasound	Ultrasound
	$f_{carrier}$ (kHz)	331	335	N/A	900000	433000	2000	1780
	Modulation	PWM Backscatter	LSK Backscatter	PGM	LSK Backscatter	OOK	LSK Backscatter	AM Backscatter
	Data Rate (kbps)	17.73	1.6	0.3	10000	6780	60	35
	Data Rate / $f_{carrier}$	0.054	0.0047	N/A	0.011	0.0156	0.03	0.0197
	Efficiency (pJ/Bit)	0.9	N/A	253	N/A	1342.2	55	603
	BER	8.5E-5 (5cm)	9E-4 (1.5cm)	N/A	5E-3 (0.8cm)	N/A	9E-5 (5 cm)	N/A
Max Distance (cm)		5	2	N/A	0.8	N/A	5	5

Figure 33.6.6: Measurement of the system's wireless neural recording over the air and *in vitro*, and comparison with state-of-the-art mm-scale wireless implants with bidirectional telemetry.

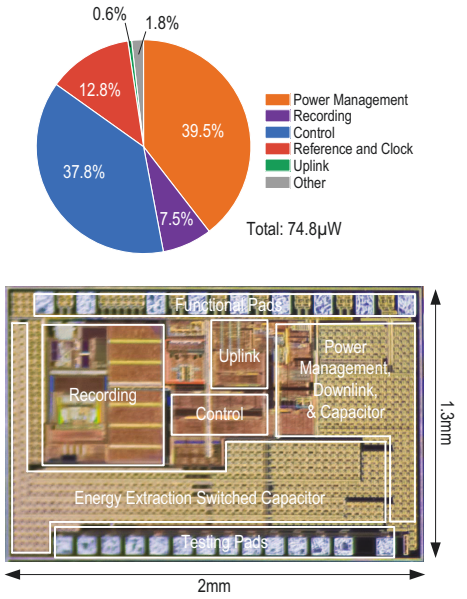

Figure 33.6.7: Implant SoC's chip micrograph and power breakdown.

Additional References:

[5] S. Hosur, et al., "Short-Range Communication for Small Biomedical Implants using Magnetoelectric Effect," *IEEE ISCAS*, May 2023.

[6] Z. Yu, et al., "Magnetoelectric Backscatter Communication for Millimeter-Sized Wireless Biomedical Implants," *MobiCom*, pp. 432-445, Oct. 2022.

[7] S. Du, et al., "An Inductorless Bias-Flip Rectifier for Piezoelectric Energy Harvesting," *IEEE JSSC*, vol. 52, no. 10, pp. 2746-2757, Oct. 2017.

[8] T.-H. Wang, et al., "A 13.8-ENOB Fully Dynamic Third-Order Noise-Shaping SAR ADC in a Single-Amplifier EF-CIFF Structure With Hardware-Reusing kT/C Noise Cancellation," *IEEE JSSC*, vol. 56, no. 12, pp. 3668-3680, Dec. 2021.

[9] J. Lim, et al., "A Light Tolerant Neural Recording IC for Near-Infrared-Powered Free Floating Motes," *VLSI Circuits Symp.*, June 2021.

[10] Y. Jia, et al., "A Trimodal Wireless Implantable Neural Interface System-on-Chip," *ISSCC*, pp. 414-415, Feb. 2020.

[11] S. Sonmezoglu, et al., "A 4.5mm^3 Deep-Tissue Ultrasonic Implantable Luminescence Oxygen Sensor," *ISSCC*, pp. 454-455, Feb. 2020.

979-8-3503-0620-0/24/$31.00 ©2024 IEEE